A New Image Reconstruction Method for Tomographic Investigation of Fluidized Beds

Shi Liu, Haigang Wang, and Fan Jiang
Institute of Engineering Thermophysics, Chinese Academy of Sciences, Beijing 100080, China

W. Q. Yang
Dept. of Electrical Engineering and Electronics, University of Manchester Institute of Science and Technology (UMIST), Manchester M60 1QD, UK

It is important to investigate the behavior of circulating fluidized beds (CFB) for efficient coal combustion. Electrical capacitance tomography (ECT) was applied to the measurement of gas/solids distribution in square CFBs. An iterative method was used to achieve improved image reconstruction over the commonly used linear back-projection algorithm. The solids concentration profile, temporal variation of average solids concentration, and frequency spectra, which were obtained from the ECT data, are presented.

Introduction

Gas/solids distribution in the bottom zone of circulating fluidized beds (CFBs) has not been well understood. Although some assumptions for the bottom region of CFB risers have been made, for example, turbulent flow and fast fluidization as opposed to bubbling fluidized bed (Grace and Lim, 1996; Werther and Hirschberg, 1996), they have not been comprehensively verified by experiments (Grace and Lim, 1996). Because the flow patterns are closely related to the gas/solids distribution in the zone, it is necessary to investigate the gas/solids distribution and to measure solids concentration profiles in this region. Unfortunately, it is difficult to make measurements on profiles, or distributions of solids concentration, due to the relatively dense and transient nature of the flow.

The recent development of electrical capacitance tomography (ECT) provides the possibility of on-line measurement of the cross-sectional solids concentration profiles in CFBs. ECT is particularly suitable for packed or dispersed gas/solids two-phase systems. It has been used to investigate pneumatic conveying and fluidization in circular geometry, and encouraging experimental results have been obtained (Halow, 1995; Wang et al., 1996; Liu et al., 1997; Williams et al., 1998; Dyakowski et al., 1997, 1999; White and Zakhari, 1999; Dyakowski and Jaworski, 2000).

Correspondence concerning this article should be addressed to W. Q. Yang.

A simplistic image reconstruction algorithm, which is commonly used, is called linear back-projection (LBP). It has been employed for CFB measurement. LBP is fast, which is essential for on-line monitoring, but performs poorly for complex distributions such as multiple objects in close vicinity. It is also difficult in reconstructing material distributions in the areas of low sensitivity, especially in the central area of the sensor. This is more pronounced if there are other objects near the measurement electrodes. For example, if there is a layer of solids near the wall of the CFB, it would be difficult to reconstruct images in the central area. The existing measurements on the bottom zone of the CFBs often display a "crown-like" solids distribution, that is, a ring of high solids fraction along the wall with an almost empty central area. Since it has been reported that the average solids concentration ranges from 35% to 40% (Svensson et al., 1996), there must be noticeable solids in the central area, raising a question about the crown-like solids distribution.

Another concern of ECT measurements on CFBs is the geometry. ECT has been applied only to circular CFBs in the past. However, the rectangular cross sections are common in CFB combustors, highlighting the need to develop a rectangular ECT system. The uncertainty of the performance of a square ECT sensor arises because of its more complicated sensitivity distributions than circular ones.

The present study is to apply an iterative algorithm in square CFB measurements. Iterative algorithms are more

powerful for complicated image reconstruction than LBP (Landweber, 1951; Isaksen, 1996; Yang et al., 1999; Liu et al., 1999). However, reports on the application of iterative methods to CFB measurement have been scarce. It will be of great interest to carry out ECT imaging of CFBs using iterative reconstruction algorithms. Square ECT sensors have been developed, for laboratory tests, jointly by UMIST and the Institute of Engineering Thermophysics of the Chinese Academy of Sciences (Yang and Liu, 1999a,b). This is the first time that comprehensive tests in real CFB environments have been reported.

Image Reconstruction

An ECT system collects capacitance data from a multielectrode sensor and reconstructs cross-sectional images from the data. The LBP algorithm uses sensitivity maps, $S_{i,j}$, and calculates the gray levels of the image elements at all locations (x, y) (that is, pixel) by the following equations

$$G(x,y) = \sum_{i=1}^{m-1} \sum_{j=i+1}^{m} S_{i,j}(x,y) C_{i,j} \Big/ \sum_{i=1}^{m-1} \sum_{j=i+1}^{m} S_{i,j}(x,y) \tag{1}$$

$$C_{i,j} = \left(C_{i,j}^{\text{mea}} - C_{i,j}^{\text{low}}\right) \Big/ \left(C_{i,j}^{\text{high}} - C_{i,j}^{\text{low}}\right)$$

where $G(x, y)$ is the gray level of the image element at location (x, y), $C_{i,j}^{\text{mea}}$ is the measured capacitance between electrode pair *i-j*, $C_{i,j}^{\text{low}}$ is the capacitance between electrode pair *i-j* when the sensing area is full of a lower permittivity material (such as empty), $C_{i,j}^{\text{high}}$ is the capacitance between electrode pair *i-j* when the sensing area is full of a higher permittivity material, $C_{i,j}$ is the normalized capacitance, m is the number of electrodes, and $S_{ij}(x, y)$ is the sensitivity of electrode pair *i-j* corresponding to an object at position (x, y).

In the preceding equations, the number of independent combinations of m electrodes is $C_m^2 = m(m-1)/2$. Since a normalized approach for the sensitivity map is adopted, each image element $G(x, y)$ is analog to a weighted average of $C_{i,j}$ with $S_{i,j}(x, y)$ acting as the weighting factors. All sensitivity elements form an $n \times C_m^2$ matrix where n is the number of pixels assigned to the sensing area. The concept of sensitivity maps is well established. General information on sensitivity maps for circular geometry is abundant in the literature, for example, Reinecke and Mewes (1997).

For convenience, Eq. 1 can be written in a vector form

$$\boldsymbol{G} = \boldsymbol{S}^T \boldsymbol{C} \tag{2}$$

where $\boldsymbol{G}$ is the image vector containing n elements of $G(x, y)$ in Eq. 1, $\boldsymbol{S}^T$ is the transpose of the normalized sensitivity map matrix, and $\boldsymbol{C}$ is the vector of all normalized capacitance.

In solids concentration measurement, image $\boldsymbol{G}$ effectively corresponds to the solids concentration profile. Although the relationship between $\boldsymbol{G}$ and $\boldsymbol{C}$ is nonlinear, LBP simplifies this problem into a linear function as an approximation. In equation (2), $\boldsymbol{C}$ contains only 66 elements for a 12-electrode ECT system, whereas normally $\boldsymbol{G}$ would contain, say 1024 (on 32×32 pixels) elements or even more. Obviously Eq. 2 is ill-posed, and such linearization would cause poor performance.

To address the nonlinear problem, there are various methods such as iterative, neural-network, and regularization. Although each method may be useful for certain problems, iterative methods are the most effective for general applications. In such a method, an image is reconstructed in an iterative manner, with a correction in each step, thus, improving the image quality progressively. There are a variety of iterative algorithms. A few examples are:

- Chen's method, which requires updating sensitivity maps for each step (Isaksen, 1996)
- Isaksen's model-based reconstruction (MOR) algorithm, which optimizes certain parameters by using a capacitance simulator and an optimization routine (Isaksen and Nordvedt, 1993)
- Reinecke's ART-like iterative method, which uses an additive function to evaluate iterative step length (Reinecke and Mewes, 1997, 1995)
- Landweber iteration (Landweber, 1951; Yang et al., 1999).

The iterative method used in this study is based on Landweber's algorithm expressed by the following equations

$$\boldsymbol{G}^{(0)} = \boldsymbol{S}^T \boldsymbol{C} \tag{3}$$

$$\boldsymbol{G}^{(k+1)} = \boldsymbol{G}^{(k)} + \alpha^{(k)} \boldsymbol{S}^T \boldsymbol{e}^{(k)} = \boldsymbol{G}^{(k)} + \alpha^{(k)} \boldsymbol{S}^T (\boldsymbol{C} - \boldsymbol{S}\boldsymbol{G}^{(k)}), \quad (k = 0,1,2,\ldots) \tag{4}$$

A first image vector is reconstructed by Eq. 3. Each subsequent image vector, $G^{(k+1)}$, is obtained from the previous image, $\boldsymbol{G}^{(k)}$, with an added correction term $\alpha^{(k)} \boldsymbol{S}^T (\boldsymbol{C} - \boldsymbol{S}\boldsymbol{G}^{(k)})$. In Eq. 4, the term $(\boldsymbol{C} - \boldsymbol{S}\boldsymbol{G}^{(k)})$ is the error between the measured capacitance, $\boldsymbol{C}$, and the calculated capacitance, $\boldsymbol{S}\boldsymbol{G}^{(k)}$. This error is used to reconstruct an error image, $\boldsymbol{S}^T(\boldsymbol{C} - \boldsymbol{S}\boldsymbol{G}^{(k)})$, which is then used to correct the next image. The process continues until a certain criterion is met, for example, $(\boldsymbol{C} - \boldsymbol{S}\boldsymbol{G}^{(k)})/\boldsymbol{C} < 0.01$. Here α is the step length, which is often chosen between 1 and 2 empirically. Too large an α will lead to divergence, and too small an α will slow down the iteration. The authors have developed an optimized method to dynamically determine α in each step, leading to fast convergence (Liu et al., 1999).

Experiment Setup

To image square channels using ECT, it is necessary to generate square sensitivity maps and to design and construct square sensors. The square sensitivity maps have been generated using finite difference solutions to the electromagnetism Laplace equations (Yang and Liu, 1999a). Details of the square sensors will be given in the subsection on CFB setup.

Stationary object setup

Experiments were carried out to evaluate the iterative image reconstruction method for square sensors first. As it is difficult to know the real gas/solids distribution in a running CFB, ECT images have to be compared with a stationary object setup for evaluation purposes. The test sensor has 12 electrodes with a measuring area of 60×60 mm. Its structure

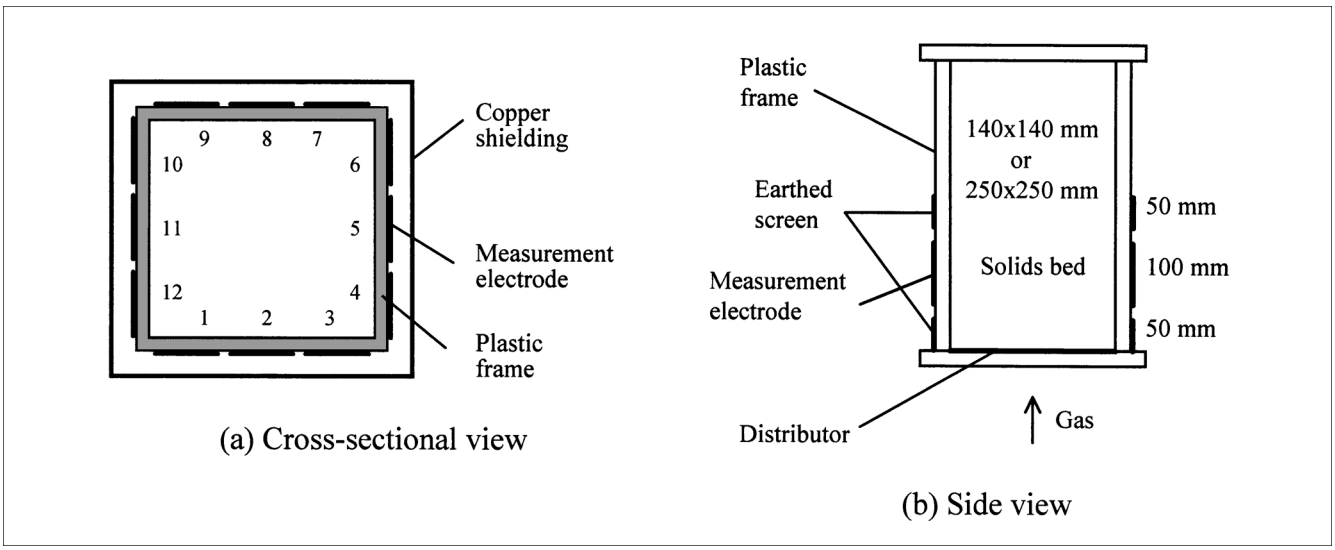

Figure 1. Square ECT sensor on a bottom zone of CFB.

is similar to those later used on CFBs, as shown in Figure 1a and 1b in the following section. It is arguable whether more measurement electrodes should be used. More independent measurements can be obtained by using more electrodes, and, hence, higher image resolution may be achieved. However, too many electrodes will reduce the size of the electrodes, and consequently the strength of the signal, resulting in a low signal-to-noise ratio (SNR). Currently a 12-electrode ECT system gives a reasonable balance between image resolution and SNR. Further details about the sensor design can be found in the literature (Yang and Liu, 1999a,b).

The test materials were plastic beads with an effective permittivity of 1.8 (Note that the effective permittivity is lower than that of the plastic material itself because of gaps between beads) and plastic rods with a permittivity of 2.6. The test materials were placed inside the sensor to get the desired distribution.

In the ECT system used for the following experiments, the data-logging electronics is controlled by a PC, which takes capacitance measurements between the sensor electrodes. A data-capture rate of 18 frames per second was chosen. Both LBP and an optimized iterative method (Liu et al., 1999) were used for image reconstruction.

CFB Setup

For the CFB tests (see Figure 2), two square beds have been built using 6-mm Perspex plates. The inner cross-sectional dimensions were 140×140 mm and 250×250 mm, respectively. Both beds have the same height of 2.8 m. The distributors consist of a perforated steel-plate grid and a mesh wire of 200 mesh beneath it. The 140×140-mm distributor has 81 holes of 6 mm in diameter, and the 250×250 mm one has 159 holes of the same diameter. The thickness of both distributors was 12 mm. The bed material was sand with a material density of 2328 kg/m^3 and a mean diameter of 0.28 mm. The loosely packed voidage was 0.43. A fixed bed was 200 mm at the beginning of every experimental run. The superficial fluidization velocity U_{mf} was chosen to cover a range from bubbling to circulating fluidization, with a minimum velocity of 0.04 m/s and a maximum velocity of 6 m/s.

The frames of the sensors are the walls of the fluidized beds. Three electrodes are mounted on each side. The width of the electrodes was modified to fit the width of each wall. The sensor is then enclosed by a grounded shielding to eliminate electric interference. The height of the measurement electrodes is 100 mm. Located both below and above the electrodes are grounded copper screens of 50 mm high.

During the experiments, LBP was used to reconstruct images for on-line monitoring, whereas the optimized iterative method (Liu et al., 1999) was used for off-line image reconstruction. In the beginning of each experiment, the ECT system was calibrated by first measuring the capacitances with an empty sensing area to obtain the lower limit, and then

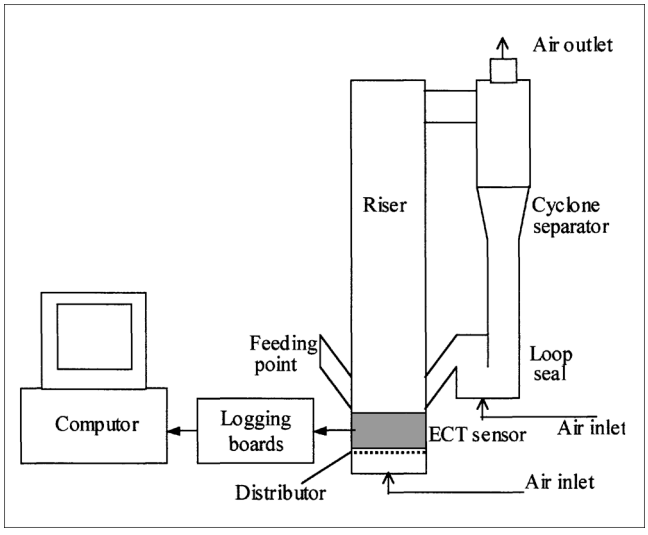

Figure 2. Experimental setup (not to scale).

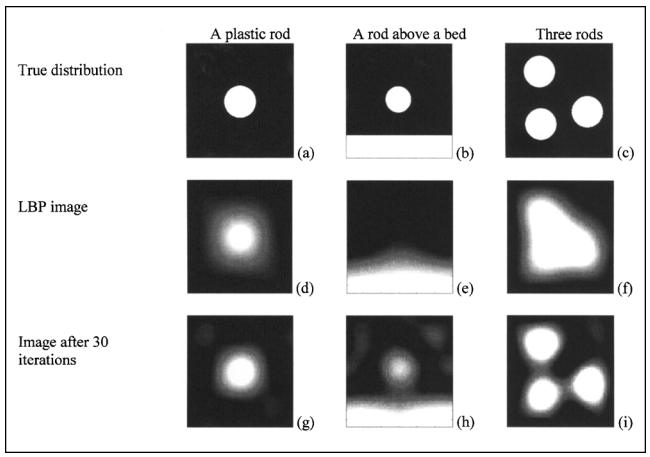

Figure 3. LBP and iterative image reconstruction for stationary objects.

measuring the capacitances with the sensing area filled with the solids to obtain the higher limit. The calibration data were stored in memory and used for the normalization of the measured capacitances.

Experimental Results

Comparison between iterative and LBP image reconstruction

Due to the scope of this article, only a limited number of experimental data are presented. Three typical results taken from stationary tests are shown in Figure 3. The sensing area is 60×60 mm. A reconstructed image represents a cross-sectional view of the objects, that is, a "slice" across the sensing plane. In the simplest case, a rod (18 mm in diameter) was placed in the center. Comparison between images (d) and (g) shows that the image reconstructed by the iterative algorithm is closer in size to the true image, and with a smaller blurred edge surrounding the object. In the other two cases, LBP is unable to show the plastic rod (10 mm diameter) above the bed (10 mm thick) of plastic beads [see image (e)], nor could it distinguish the three plastic rods (18 mm in diameter) [see image (f)]. In contrast, the iterative method clearly presents the objects [see images (h) and (i)].

The significance of image (h) is that the iterative method can display materials both near the wall and in the center, which is a particular weakness of LBP. Image (i) further shows the better resolution of the iterative method than LBP.

Figure 4 shows six typical cases in different fluidized-bed conditions. The minimum superficial fluidization velocity, U_{mf}, is 0.04 m/s. The fluidization conditions are also given in the plots. Images (a), (b), (c), (d), (e), and (f) show two cases of high solids fraction. In images (a) and (d), the red color represents solids and the blue color represents voids (that is, air bubbles). Images (b) and (e) are contour maps of the concentration, and each circled line represents a concentration level. In surface-map images (c) and (f), the elevations of the surface also represent the solids concentration levels. Comparing the images by LBP with those by the iterative method, the iterative images show smaller bubbles and slightly higher solids fraction in the central area. This result indicates that

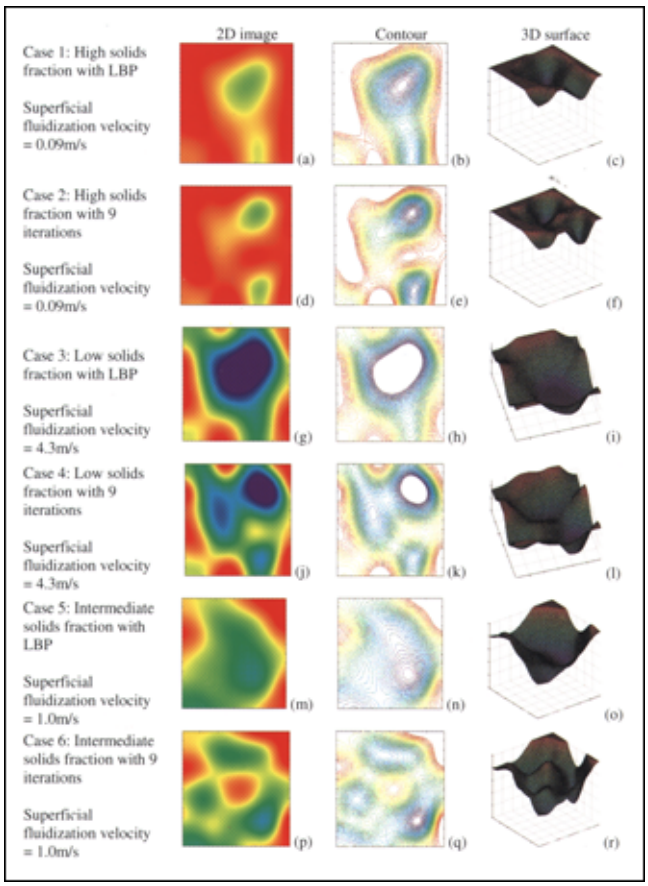

Figure 4. Solids distributions in bottom zone of CFB.

LBP can be used in dense-phase image reconstruction, when the measurement signals are so strong that the relatively low sensitivity away from the electrodes becomes less of a problem.

Images (g), (h), (i) and (j), (k), (l) demonstrate two cases of relatively low solids concentration. In image (g) reconstructed by LBP, only one large bubble can be seen near the central area. The surface image (i) presents a crown-like solids fraction distribution with a single void near the center, which agrees with those for circular geometry in the previous literature. Comparing these images with images (e) and (h) in Figure 3, where the objects were not separated in the image, we see that we are unable to distinguish closely positioned objects in any of them, either higher permittivity objects in a lower permittivity background (rods in Figure 3) or lower permittivity objects in a higher permittivity background (bubbles in Figure 4). In contrast, improved results by iterative image reconstruction indicate higher solids fractions in some parts of the central area, and several bubbles are identified instead of only one, as shown in images (j), (k), and (l) in Figure 4. This coincides with the improved images using the iterative method in images (f) and (i) in Figure 3.

Two cases for intermediate solids fractions are presented by images (m), (n), (o), (p), (q), and (r) in Figure 4. Essentially, the characteristics are similar to the preceding ones. In images (m), (n), and (o) reconstructed by LBP, a large void appears in the center. However, images (p), (q), and (r) re-

constructed by the iterative method demonstrate significantly higher solids fraction in the center, together with several bubbles around the edges.

In summary, the iterative algorithm can reconstruct more detailed solids concentration profiles in the bottom zone of the CFB risers than LBP can. The distributions agree with the common opinion that the bottom region is bubbling or turbulent. However, images reconstructed by LBP appear to have neglected some solids areas in the middle, reflecting the deficiency of LBP.

Solids concentration characteristics in bottom zone of CFBs

As the flow rate of the fluidization air increases, the fluidization condition evolves through several stages from bubbling to circulating fluidization. The following part presents three characteristic cases, namely, bubbling, slugging, and circulating fluidization.

In each experiment, 1,000 data were sampled in 55 s. Solids distribution profiles were reconstructed from the data. Meanwhile, the average solids concentrations over the cross section, λ, were calculated from the solids concentration distribution. The results are summarized in Table 1, showing the mean λ, the standard deviation (std) in λ, and the maximum and minimum λ. Two sets of data are listed for each flow regime under the same operating conditions.

Bubbling Fluidized Bed. For bubbling fluidization tests, the superficial fluidization velocity was 0.09 m/s. The gas/solids distribution is shown in Figure 5. Bubbles appear throughout the bed. The solids concentration profile is similar to that for high solids concentration in Figure 4d. The solids distribution (or the position), the size, and number of the bubbles can be seen, which provides information on the fluidization characteristics.

From the ECT data, the history of the events in the bed can be observed. In Figure 5, the air fraction increases from images (1) to (6) and decreases from images (7) to (10). Such a pattern repeats over the time, from which the frequency of bubble occurrence can be estimated. From Figure 5, it appears that 10 frames of images take 0.55 s to complete one passage of the bubbles. This corresponds to 1.8 Hz in frequency.

In addition to the information in spatial distribution, the characteristics of λ and its temporal variation are important because (1) it is a parameter for the design and operation of CFBs, and (2) like pressure measurements, λ can reflect the flow fluctuations or the dynamic behavior of the bed. In Table 1, λ ranges from 29.2% to 56.8% for the first case and 24.7% to 56.8% for the second case, with mean values of 51.4% and 50.6%, respectively.

Table 1. Statistical Characteristics of Three Fluidization Regimes

	Bubbling		Slugging		Circulating	
	Case-1	Case-2	Case-3	Case-4	Case-5	Case-6
Mean λ	0.514	0.506	0.338	0.35	0.225	0.229
Std.	0.0581	0.0618	0.0925	0.0876	0.0425	0.045
Max. λ	0.568	0.568	0.563	0.561	0.387	0.432
Min. λ	0.292	0.247	0.1	0.148	0.111	0.118

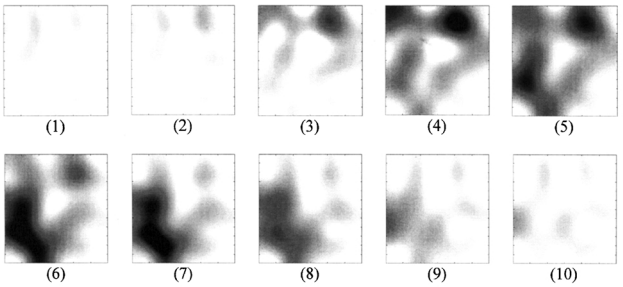

Figure 5. Cross-sectional solids concentration in bottom of bubbling bed.

Black color is the highest voidage.

The preceding data are comparable with an earlier investigation that used both a pressure sensor and an ECT sensor on a circular fluidized bed (Liu et al., 1997). In the previous study, the mean λ ranged from 50% to 56% by pressure measurement, and from 47% to 57% by circular ECT measurement in the bubbling fluidization regime. The data from this study lie within the range just given.

It has been reported that the pressure fluctuations in the bottom of the bed occur at 0.5 and 1.4 Hz (Svensson et al., 1996). For comparison purposes, fast Fourier transform (FFT) is performed on λ to obtain its frequency spectra. The results are shown in Figure 6.

Figure 6a shows the variation of λ with time between 30% and 57% (the low values corresponding to large air fractions). There are 1,000 data sampled over a time period of 55 s. To view it more clearly, Figure 6b shows the selected data from the first 10 s, in which the periodic nature of the curve can be seen. The frequency spectrum from FFT is shown in Figure 6c, which clearly illustrates a peak corresponding to a frequency of about 1.6 Hz. This result agrees with that from the pressure measurement of Svensson et al. (1996). Although Svensson's low frequency of 0.5 Hz does not appear here, one reason for it may be the different geometry of the fluidized beds and a different operating temperature. In the Svensson study, the bed was 1.47×1.42 m and the temperature was 850°C.

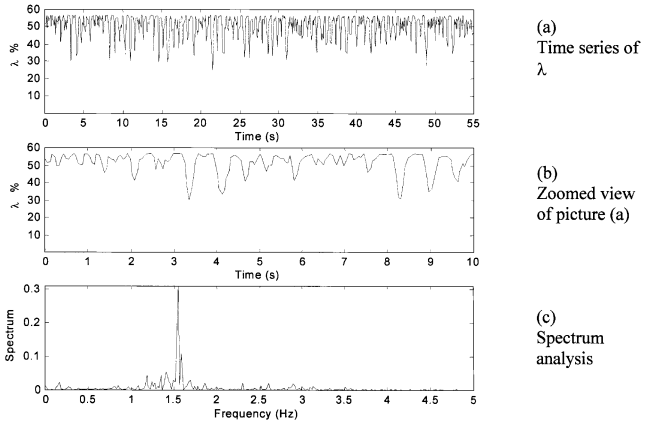

Figure 6. Average concentration and frequency spectrum in bubbling bed.

Werther and Molerus (1973a,b) used needle-type sensors to measure the bubble velocity and the mean number of bubbles that struck the sensor per unit time, at different heights above the distributor and radial locations in circular fluidized beds. When the height was 8 cm, the volume fraction of the bubbles was found to be particularly high in an annular region close to the wall. In Figure 5 (4)–(7) and Fig.4 (p), (q), and (r), the ECT images show qualitatively an annular region wherein more bubbles occur than in other regions. This suggests certain similarities to Werther and Molerus' measurements, though they are far less regular. Therefore, further studies are needed to verify these discoveries. Moreover, in our case there are often high solids concentrations in the corners of the bed, which is a good demonstration of a special feature of square beds. Also, according to Werther and Molerus' data, the mean number of bubbles that struck the sensor per unit time ranged from about 0.5 to 3–4, a large number being within 1 to 2. This may be compared with our case, that is, about 1.6 Hz.

Slugging Bed. The images reconstructed for slugging fluidization are shown in Figure 7, which correspond to a superficial fluidization velocity of 1.5 m/s. Slugging occurred when bubbles grew to sizes similar to the cross section of the bed. It is well known that slugging fluidization is characterized by the largest pressure fluctuations. In our measurements it corresponded to the largest fluctuations in solids concentration profiles. Our measurements focused on the characteristics of the solids distribution in the slugging bed, instead of the unset point of slugging. Therefore, images presented in this article correspond to the condition wherein the largest fluctuation in solids concentration occur. The images show large variations in the gray level, for example, images (2) and (5). There are conditions like bubbling fluidized bed with scattered bubbles, as well as conditions when the majority of the bed is occupied by large voids. In Figure 7, solids concentration decreases from image (1) to a minimum at image (7). It then increases until image (12) is reached, and starts to fall again until it reaches image (16). It further increases toward image (20). This again shows its periodical nature.

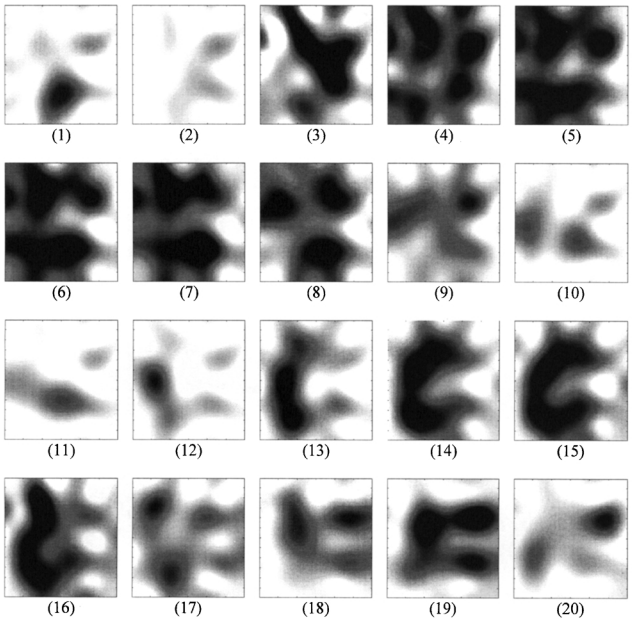

Figure 7. Cross-sectional solids concentration in bottom of slugging bed.

Black color is the highest voidage.

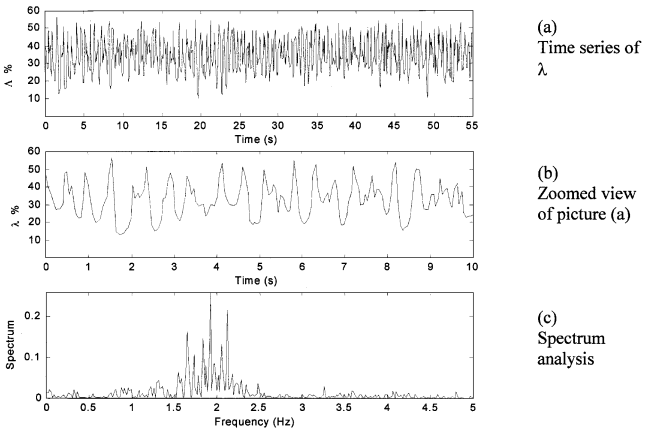

Figure 8. Average concentration and frequency spectrum in slugging bed.

The temporal variation of mean λ with time and its frequency spectrum are shown in Figure 8. Compared with Figure 6, the overall solids concentration is lower in the slugging bed, but the fluctuation is stronger (roughly from 10% to 57%) than the bubbling bed. This is also shown in Table 1, in which λ varies from 10% to 56.3% in one case, and from 14.8% to 56.1% in the other, with mean values of 33.8% and 35%, respectively. These data are also comparable with the previous study (Liu et al., 1997) in which λ ranged from 37% to 48% by pressure measurement, and from 24% to 41% by circular ECT measurement. The higher value by pressure measurement than by ECT may be due to the effect of solids acceleration in the slugging zone, which affects pressure measurements, but not ECT data.

The frequency spectrum by FFT shown in Figure 8c indicates a few peaks around 1.6–2.2 Hz, with the highest peak at 1.9 Hz.

Circulating bed. The images of solids distribution in a circulating bed are shown in Figure 9 and correspond to a superficial fluidization velocity of 4.3 m/s. The velocity exceeded the transport velocity (Basu and Fraser, 1991) by a considerable margin. This means that the condition was in

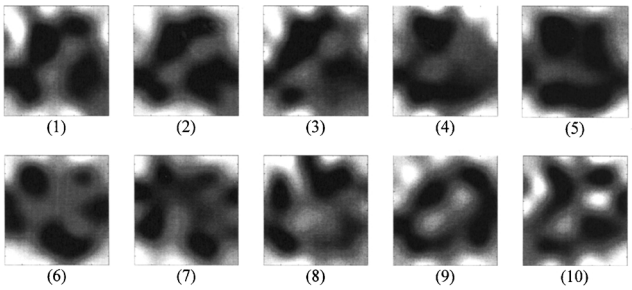

Figure 9. Cross-sectional solids concentration in bottom of circulating bed.

Black color is the highest voidage.

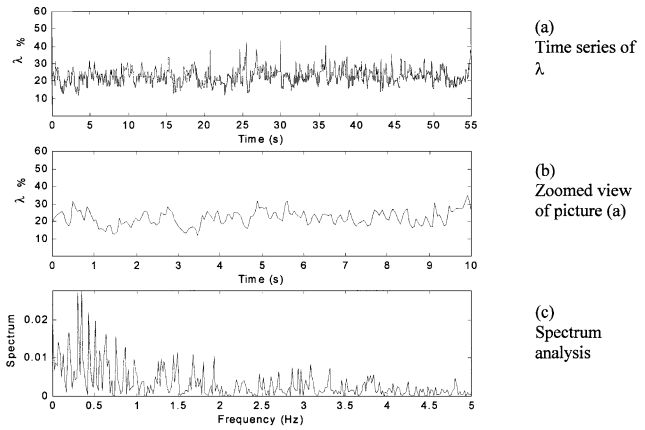

Figure 10. Average concentration and frequency spectrum in circulating bed.

the fast fluidization regime. A distinctive feature is the large voids over the cross section. Meanwhile, solids clusters, that is, the white patches, are clearly visible in the central area, which provides more information than do images reconstructed by LBP. This again shows the advantage of the iterative image reconstruction algorithm. The improvement is significant in the bottom zone, whereas in the upper part of a CFB riser, the crown-like solids distribution is reasonable.

The temporal variation of mean λ with time and its frequency spectrum are shown in Figure 10. Figure 10a shows that λ ranges from 10% to 40%, substantially lower than the bubbling bed. Table 1 shows the same feature, in which λ ranges from 11.1% to 38.7% in the first case and 11.8% to 43.2% in the second case, with a mean λ of 22.5% and 22.9% respectively.

The data can be compared with those in the literature. For example, Kunii and Levenspiel (1991) gave the value of solids fractions in the lower dense region of CFBs as 16–22%, and Basu and Fraser (1991) gave 0.12–0.22%, compared to the 22.5 and 22.9% that were obtained from the ECT data.

The frequency spectrum in circulating fluidization is more irregular than those in bubbling and slugging fluidizations. The peaks occur mostly below 2 Hz, with the highest peak at 0.3 Hz. This feature reflects the chaotic flow pattern in the circulating fluidization or its relatively weak periodicity. This pattern can be compared with the less distinct periodic variation of the flow pattern in Figure 9. The low frequency peak at 0.3 Hz indicates large bubbles or the prolonged time it takes for the air bubbles to pass. The irregularity may be caused by insufficient data. To analyze the low-frequency phenomenon, it seems that more data over longer periods of time are needed. Therefore, the preceding speculations need to be investigated further.

Conclusions and discussion

Measurement of the solids concentration in the bottom zone of CFB risers using LBP often produces a crown-like profile, which tends to lose information on the solids distribution in the central area. The iterative image-reconstruction method can measure the solids concentration in square CFBs more accurately than LBP can.

The results reveal noticeable solids fraction in the central region of the CFBs. This agrees with the nature of bubbling or turbulent fluidization in the bottom zone. Meanwhile, closely distributed multiple voids (gas bubbles) can be distinguished. Such results correspond well to those from the experiments on the stationary objects.

In the bubbling fluidization regime, λ varies between 24% to 57%, with a mean λ of 51% and a peak at 1.6 Hz in the frequency spectrum. In the slugging fluidization regime, the fluctuation is much larger than in the bubbling and circulating fluidized beds. In the addition, λ varies between 10% and 56%, with a mean λ of 34% and a peak at 1.9 Hz in the frequency spectrum. In the circulating fluidization regime, λ becomes much lower than in the other two regimes, in a range from 11% to 43%, with a mean λ of 23%, plus the frequency spectrum is more complicated, with an apparent peak of about 0.3 Hz.

The square ECT system has been successfully used in imaging the bottom zone of CFBs. The data obtained are valuable references for further studies. With rapidly growing computer speed, on-line iterative reconstruction is expected to be available in the near future. The capability of ECT in providing simultaneous spatial and temporal information on two-phase flow is unique, and can be of immense value in the study of fluidization processes.

As a new technology, ECT has not been applied to large-scale facilities. Some problems must be addressed before ECT can be tested on large geometries. First, the electronic circuits must be designed to provide a relatively large charge current and to use long signal cables. Second, image reconstruction methods for ECT must be improved for higher resolution and accuracy, as they are lower than some other tomographic techniques such as gamma-ray tomography. This involves a trade-off between high speed, high accuracy, and low cost. Third, the sensors must be more carefully designed and fabricated for a high SNR, and to reduce electrical interference from the outside.

Acknowledgments

The authors thank the British Council for sponsoring the Academic Link with China Scheme (PEK\0992\311), which has resulted in fruitful research through the collaboration between the Institute of Engineering Thermophysics of the Chinese Academy of Sciences and UMIST, UK. The National Natural Science Foundation of China is also thanked for funding the research (No. 50076045).

Notation

$\boldsymbol{C}$ = normalized capacitance vector
$C_{i,j}$ = normalized capacitance between electrode pair *i-j*
$C_{i,j}^{\text{mea}}$ = measured capacitance between electrode pair *i-j*
$C_{i,j}^{\text{low}}$ = capacitance between electrode pair *i-j* when the sensing area is full of a lower permittivity material
$C_{i,j}^{\text{high}}$ = capacitance between electrode pair *i-j* when the sensing area is full of a higher permittivity material
$\boldsymbol{E}$ = electric field, V/m
$\boldsymbol{G}$ = image vector
$G(x,y)$ = gray level of the image element at location (x, y)
i, j = capacitance pair index
k = iteration number
m = number of electrodes
n = number of pixels assigned to the sensing area
$p(x,y)$ = area of pixel (x, y), m^2

$\boldsymbol{S}$ = normalized sensitivity-map matrix
$\boldsymbol{S}^T$ = transpose of normalized sensitivity-map matrix
$S_{i,j}(x, y)$ = sensitivity of electrode pair *i-j* corresponding to an object at position (x, y)
U_{mf} = minimum superficial fluidization velocity, m/s
V = voltage, V
x, y = orthogonal coordinates, m

Greek letters

α = iteration step length
ϵ = relative material permittivity
λ = average solids concentration in cross section
ϕ = electric potential, V

Literature Cited

Basu, P., and S. A. Fraser, *Circulating Fluidized Bed Boilers: Design and Operation*, Butterworth-Heinemann, Boston (1991).

Dyakowski, T., R. B. Edwards, C. G. Xie, and R. A. Williams, "Application of Capacitance Tomography to Gas-Solid Flows," *Chem. Eng. Sci.*, **52**, 2099 (1997).

Dyakowski, T., S. P. Luke, K. L. Ostrowski, and R. A. Williams, "On-Line Monitoring of Dense Phase Flow Using Real Time Dielectric Imaging," *Powder Technol.*, **104**, 287 (1999).

Dyakowski, T., and A. J. Jaworski, "Application of Tomographic Techniques for Imaging Fluidized Beds," *Proc. Israeli Conf. for Conveying and Handling of Particulate Solids*, Dead Sea, Israel, p. 15.1 (2000).

Grace, J. R., and K. Lim, "Reactor Modeling for High-Velocity Fluidized Beds," *Circulating Fluidized Beds*, J. R. Grace, A. A. Avidan, and T. M. Knowlton, eds., Blackie, London, p. 1 (1996).

Halow, J. S., "Capacitance Imaging of Fluidized Beds," *Process Tomography: Principles, Techniques and Applications*, R. A. Williams, and M. S. Beck, eds., Butterworth Heinemann, Oxford, p. 447 (1995).

Isaksen, Ø., "A Review of Reconstruction Techniques for Capacitance Tomography," Meas. Sci. Technol. **7**, 325 (1996).

Isaksen, Ø., and J. E. Nordtvedt, "A New Reconstruction Algorithm for Process tomography," *Meas. Sci. Technol.*, **4**, 1464 (1993).

Kunii, D., and O. Levenspiel, *Fluidization Engineering*, 2nd ed., Butterworth-Heinemann, Boston (1991).

Landweber, L., "An Iterative Formula for Fredholm Integral Equations of the First Kind," *Amer. J. Math*, **73**, 615 (1951).

Liu, S., S. Wang, D. J. Mason, T. Dyakowski, and D. Geldart, "Measurement of Solids Concentration in Gas-Solid Flows Using Capacitance Tomography and Pressure Sensors," *Sensors and Their Applications VIII*, A. T. Augousti, and N. M. White, eds., Institute of Physics Publishing, Bristol and Philadelphia, p. 101 (1997).

Liu, S., L. Fu, and W. Q. Yang, "Optimisation of an Iterative Image Reconstruction Algorithm for Electrical Capacitance Tomography," *Meas. Sci. Technol.*, **10**, L37 (1999).

Reinecke, N., and D. Mewes, "Investigation of the Two-Phase Flow in Trickle-Bed Reactors Using Capacitance Tomography," *Chem. Eng. Sci.*, **52**, 2111 (1997).

Reinecke, N., and D. Mewes, "Improvement of Linearity and Resolution of Multielectrode Capacitance Sensors for the Tomographic Visualization of Transient Two-Phase Flows," *Flow Visualization and Image Processing of Multiphase Systems*, 259 (1995).

Svensson, A., F. Johnsson, and B. Leckner, "Bottom Bed Regimes in a Circulating Fluidized Bed Boiler," *Int. J. Multiphase Flow*, **22**, 1187 (1996).

Wang, S., T. Dyakowski, and M. S. Beck, "An Application of Electrical Capacitance Tomography to Measure Gas-Solid Motion in Fluidized Bed," *Heat-Transfer*, AIChE Symp. Ser., Houston, p. 155 (1996).

Werther, J., and B. Hirschberg, "Solids Motion and Mixing," *Circulating Fluidized Beds*, J. R. Grace, A. A. Avidan, and T. M. Knowlton, eds., Blackie, London, p. 119 (1996).

Werther, J., and O. Molerus, "The Local Structure of Gas Fluidized Beds—I. A Statistically Based Measuring System," *Int. J. Multiphase Flow*, **1**, 103 (1973a).

Werther, J., and O. Molerus, "The Local Structure of Gas Fluidized Beds—II. The Spatial Distribution of Bubbles," *Int. J. Multiphase Flow*, **1**, 123 (1973b).

White, R. B. and A. Zakhari, "Internal Structures in Fluid Beds of Different Scales: An Application of Electrical Capacitance Tomography," *Proc. 1st World Congress on Industrial Process Tomography*, Buxton, UK, p. 39 (1999).

Williams, R. A., S. P. Luke, K. Ostrowski and T. Dyakowski, "Real Time Imaging of Dense Phase Particulate Flows in Conveying and Fluidization," *Int. Symp. on On-Line Flow Measurement of Particulate Solids*, Univ. of Greenwich, Chatham, UK, p. 172 (1998).

Yang, W. Q., D. M. Spink, T. A. York and H. McCann, "An Image Reconstruction Algorithm Based on Landweber Iteration Method for Electrical Capacitance Tomography," *Meas. Sci. Technol.*, **10**, 1065 (1999).

Yang, W. Q. and S. Liu, "Electrical Capacitance Tomography with a Square Sensor," *Proc. 1st World Congress on Industrial Process Tomography*, Buxton, UK, p. 313 (1999a).

Yang, W. Q., and S. Liu, "Electrical Capacitance Tomography with Square Sensor," *Electron. Lett.*, **35**, 295 (1999b).

Manuscript received June 29, 2001, and revision received Jan. 28, 2002.